ACS OMEGA

Open Access

http://pubs.acs.org/journal/acsodf

Article

Preliminary Exploration of Pseudo-CT-Based Attenuation Correction for Simultaneous PET/MRI Brain Imaging in Nonhuman Primates

Chi-Hyeon Yoo,[#] Jonathan M. DuBois,[#] Lu Wang,[#] Yongjin Tang, Lu Hou, Hao Xu, Jiahui Chen, Steven H. Liang, David Izquierdo-Garcia,[*] and Hsiao-Ying Wey[*]

Cite This: *ACS Omega* 2023, 8, 45438−45446

Read Online

ACCESS | Metrics & More | Article Recommendations | Supporting Information

ABSTRACT: This study aimed to develop a template-based attenuation correction (AC) for the nonhuman primate (NHP) brain. We evaluated the effects of AC on positron emission tomography (PET) data quantification with two experimental paradigms by comparing the quantitative outcomes obtained using a segmentation-based AC versus template-based AC. Population-based atlas was generated from ten adult rhesus macaques. Bolus experiments using [^{18}F]PF-06455943 and a bolus-infusion experiment using [^{11}C]OMAR were performed on a 3T Siemens PET/magnetic resonance-imaging (MRI). PET data were reconstructed with either μ map obtained from the segmentation-based AC or template-based AC. The standard uptake value (SUV), volume of distribution (V_T), or percentage occupancy of rimonabant were calculated for [^{18}F]PF-06455943 and [^{11}C]OMAR PET, respectively. The leave-one-out cross-validation showed that the absolute percentage differences were 2.54 ± 2.86% for all region of interests. The segmentation-based AC had a lower SUV and V_T (∼10%) of [^{18}F]PF-06455943 than the template-based method. The estimated occupancy was higher in the template-based method compared to the segmentation-based AC in the bolus-infusion study. However, future studies may be needed if a different reference tissue is selected for data quantification. Our template-based AC approach was successfully developed and applied to the NHP brain. One limitation of this study was that validation was performed by comparing two different MR-based AC approaches without validating against AC methods based on computed tomography (CT).

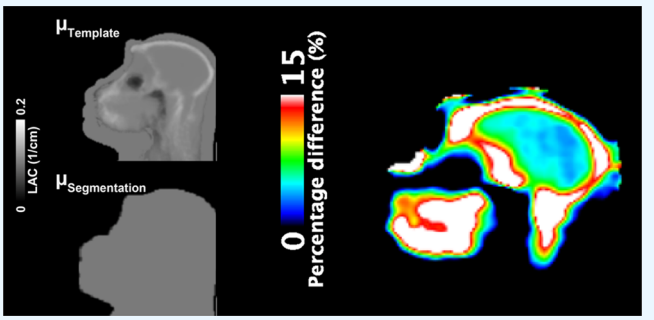

INTRODUCTION

Positron emission tomography (PET) is a sensitive molecular imaging tool allowing quantification of target availability when appropriate radioligand(s) exists.[1] Characterization and validation of novel radioligands that bind to a specific molecular target in the brain of nonhuman primates (NHPs) could facilitate the successful translation of such a molecular imaging tool from preclinical development to clinical application in humans.[2] PET imaging in NHP brains provides several translational benefits. First, it is feasible to perform arterial blood sampling in large NHPs, such as rhesus macaques or baboons, for quantitative analysis of PET data using kinetic modeling methods, which are usually unavailable for rodents. Tracer kinetic parameters, including micro- and macro-parameters, and the specific binding of the tracer can be estimated *in vivo*, which may closely resemble the pharmacokinetic and pharmacodynamic properties of the novel PET tracer in the human brain.[2] Second, it is feasible to measure the occupancy of drugs/compounds to the selective target systems *in vivo* by performing a set of baseline-blocking scans at multiple doses to establish a dose−response relationship in a clinically relevant large animal model.[3] The resulting dose-occupancy information can offer better dose extrapolation for human studies considering the phylogenetic proximity of NHPs to humans.[4] Collectively, PET imaging in NHP brains plays an important role in the *in vivo* evaluation of newly developed radiotracers and drugs for translation research.

Integration of PET and magnetic resonance imaging (MRI) offers unique opportunities to synergize the molecular imaging capability of PET and the anatomic and functional imaging capability of MRI.[5,6] For example, MR-based partial volume correction and motion correction methods have been applied to improve PET quantification.[7,8] Besides the technical advances of PET/MRI, functional PET/MRI studies with pharmacological[9,10] and behavioral/task interventions have demonstrated novel applications to investigate brain function.[11,12] With these benefits, a simultaneous PET/MRI system

Received: July 5, 2023
Accepted: September 14, 2023
Published: November 17, 2023

has been increasingly utilized for brain imaging research.[7,13] However, one of the major challenges for PET/MRI systems is providing an accurate attenuation correction (AC) for the emission scan of PET, which is essential for accurate quantitative mapping.[14] Due to the lack of direct association between MR signals and photon attenuation in the objects, it has been challenging to derive the linear attenuation coefficients (LACs) from MR signals.

Among MR-based AC methods, we have previously demonstrated the use of a template-based approach that combines segmentation and nonrigid registration to a template, and that has been applied to several human brain PET studies with reliable performance.[15−17] In brief, the template-based AC method segments the structural MRI scans into distinct tissue classes and subsequently registers the tissue classes with corresponding classes of a predefined template. The performance of this method was superior to other MR-based AC methods, such as DIXON or ultrashort-TE, and comparable to the gold standard as CT-based AC,[15] and independently evaluated and elected among the top-3 human brain MR-AC methods by an international study.[18] Recently, increasing numbers of machine learning or deep learning approaches have actively been worked on as another method of choice for deriving AC maps for PET/MRI. However, to date, all the established MR-based AC methods are optimized for the human brain.[17] Due to differences in morphology, size, and MR contrast between human and NHP brains, data acquisition as well as imaging processing methods require careful optimization for the implementation of MR-based AC to the NHP brain. An accurate AC method for NHP brains is essential to reduce bias in PET data quantification, which is particularly important when characterizing novel PET radiotracers and measuring target occupancy.

This study aimed to develop and optimize a template-based AC method for the NHP brain using a pipeline similar to our previous work in humans. We evaluated the effects of AC methods on PET data quantification using kinetic modeling with two dynamic PET paradigms, i.e., a set of baseline/blocking experiments with bolus injection of PET radiotracer and a bolus-infusion (B/I) paradigm of PET radiotracer with a within-scan drug challenge. We compared a segmentation-based AC method with our template-based AC approach using two experimental paradigms: (1) Utilizing the novel radiotracer [^{18}F]PF-06455943, baseline-blocking PET scans were acquired with arterial blood samples on two separate imaging sessions. The [^{18}F]PF-06455943 radiotracer was previously used in the NHP brains and demonstrated favorable kinetic properties for the calculation of kinetic parameters using the two-tissue compartment (2TCM) and favorable volume of distribution (V_T) displacement of 45−55% throughout the brain by the homologous blocking.[19,20] (2) We performed a B/I study using the radiotracer [^{11}C]OMAR, which binds to cannabinoid type 1 receptor (CB1R) while administering an antagonist (rimonabant). In the B/I study, the receptor occupancy of an antagonist was determined. In addition to investigating the impact of AC methods on PET quantification with two different experimental paradigms, we evaluated the potential effects of misregistration of tissues outside the brain as a result of the increased anatomical variability of NHP heads compared to humans. We hypothesized that a template-based AC method for the NHP brain can be successfully established, and the template-based AC method will increase PET signal intensity compared with a segmentation-based method by properly considering realistic structures, e.g., bone and air. Furthermore, we anticipated that the effects of AC would introduce a larger bias in PET quantification with the two-scan paradigm, i.e., baseline/blocking studies with arterial sampling than the occupancy estimation on the B/I scan using a within-scan drug challenge.

RESULTS AND DISCUSSION

This study developed and optimized an NHP template-based approach to generate pseudo-CT (pCT) images, which we then tested in a series of studies using PET tracers with dynamic PET/MR. As previously proposed,[15] segmentation- and template-based approaches were combined and adapted to segment tissue classes to facilitate a robust AC method for NHP brain imaging. Population-based CT-MRI templates were generated by coregistering pairs of MRI and CT images of NHPs. Figure 1 shows the six classes of tissue images, MRI,

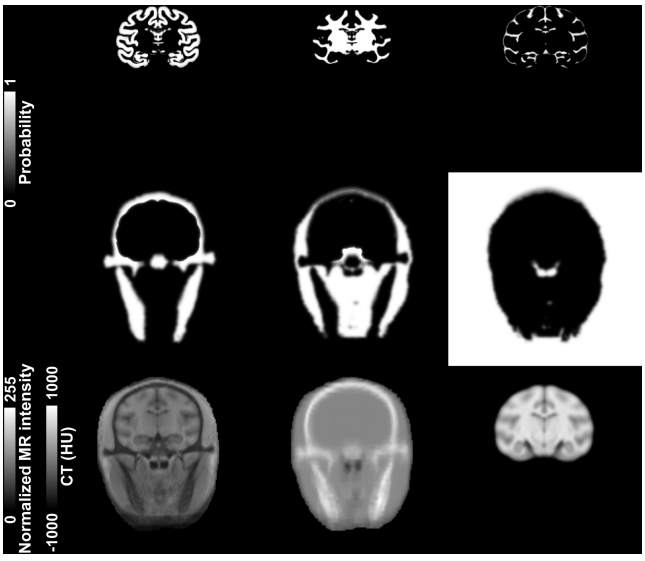

Figure 1. Template images generated from ten rhesus monkeys. Tissue classes obtained from the final iteration of diffeomorphic nonrigid coregistration method (top and middle row). From left to right are gray matter, white matter, and cerebrospinal fluid (top row) and bone, soft tissue, and air (middle row). Template MRI (left) and CT (middle) images and INIA19 primate brain atlas (right) were used for region-based analysis (bottom row). Magnetic resonance imaging, MRI; computed tomography, CT.

and CT templates generated from the atlas-generation data set using the Statistical Parametric Mapping 8 software (SPM8; Wellcome Trust Centre for Neuroimaging, University College London) Diffeomorphic Anatomical Registration Through Exponentiated Lie Algebra (DARTEL) together with the INIA19 template.[21] The leave-one-out cross-validation (LOOCV) results from a representative NHP showed an agreement within brains despite discrepancies in the spout region when the attenuation correction map derived from actual CT (μ_{CT}) and the generated CT ($\mu_{Template}$) were compared (Figure 2). The LOOCV results of the template-based method in the atlas-generation data set showed that the mean absolute percentage difference (%PD) was 4.58 ± 3.11% for all brain voxels and 2.54 ± 2.86% for all ROIs. Supporting Figure 1 shows the Bland−Altman plots for the voxel-based analyses for all validation subjects, comparing μ_{CT} and $\mu_{Template}$. When $\mu_{Segmentation}$ was compared with μ_{CT} in the atlas-

https://doi.org/10.1021/acsomega.3c04824
ACS Omega 2023, 8, 45438−45446

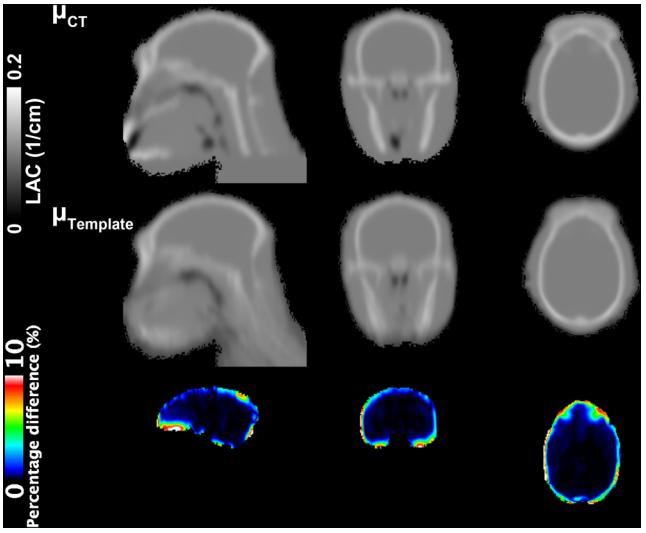

Figure 2. Attenuation maps derived from the actual CT (μ_{CT}), the generated CT ($\mu_{Template}$), and their percentage differences are displayed in 3 orientations. Computed tomography, CT.

generation data set, obvious misclassification of bone and air was shown in the segmentation-based AC. Consistently, a slightly higher mean %PD was found for the segmentation-based method, 10.04 ± 2.74% for all brain voxels and 6.55 ± 5.27% for all ROIs, compared to the template-based approach. Figure 3 shows the μ maps obtained with the two AC methods

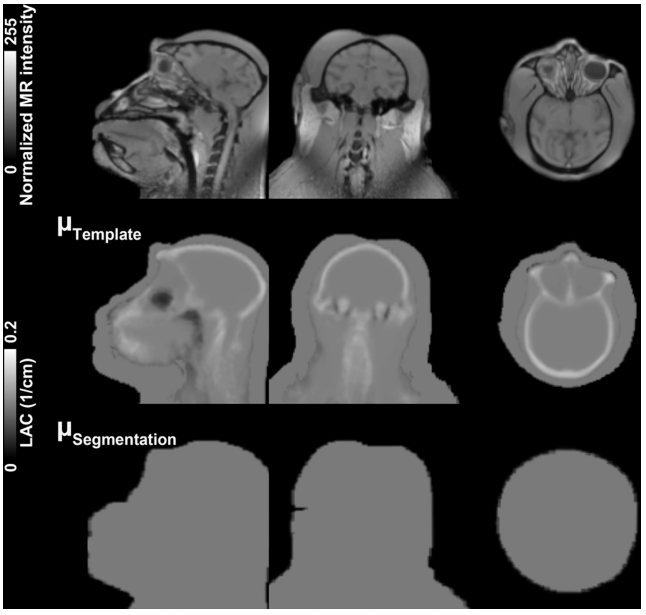

Figure 3. Structural MRI scan and attenuation maps with obtained by the template approach ($\mu_{Template}$) and a segmentation-based AC method ($\mu_{Segmentation}$) from a representative monkey. Magnetic resonance imaging, MRI; attenuation correction, AC.

for the same macaque. It is apparent that bone and air tissues are misidentifications in the $\mu_{Segmentation}$ map[22] but not in the $\mu_{Template}$ map when compared with the anatomical MRI visually.

We tested the performance of the proposed AC method for PET scans in the NHP brain using a novel tracer, [^{18}F]PF-06455943, with arterial blood samples in the context of quantitative PET studies that aim to evaluate novel radiotracers. The reconstructed standardized uptake value (SUV) images of [^{18}F]PF-06455943 were compared between the segmentation-based ($SUV_{1-10\ min,\ Segmentation}$) and template-based AC methods ($SUV_{1-10\ min,\ Template}$) in a representative macaque (Figure 4). As shown in the %ΔSUV map, the

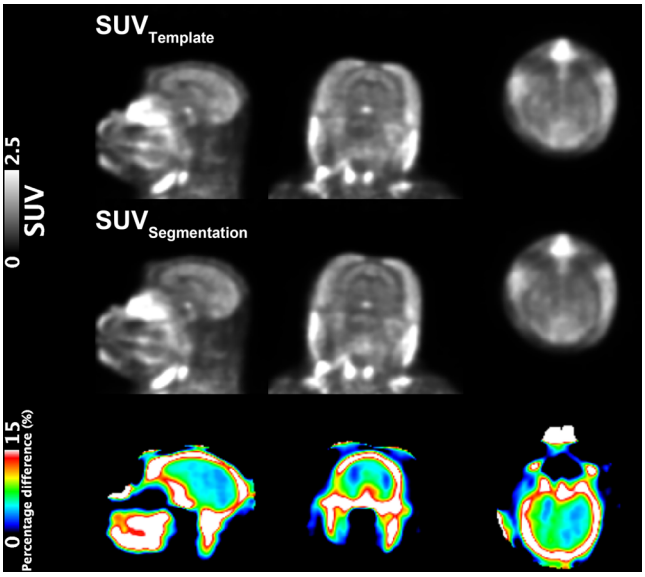

Figure 4. PET images reconstructed with the 2 AC methods ($SUV_{Template}$ and $SUV_{Segmentation}$) for a [^{18}F]PF-06455943 baseline scan (top and middle row) and their percentage differences (bottom row). Positron emission tomography, PET; attenuation correction, AC; standard uptake value, SUV.

segmentation-based AC method showed lower SUV (~10%) within the brain when compared to the template-based AC method. The region-based comparison of the estimated V_T values for each AC method is summarized in Figure 5 and Table S1. For baseline scans, the segmentation-based AC method showed lower V_T (3.77 ± 0.46 mL/cm^3 averaged from 19 ROIs excluding whole brain) than those derived using the template-based AC method (4.13 ± 0.49 mL/cm^3 averaged from 19 ROIs), and their average percentage differences were 9.40 ± 3.22%. Similarly, V_T was lower with the segmentation-based AC method compared with the template-based approach, with mean percentage differences of 7.79 ± 4.43%. Consistent with the previous findings,[15] the most significant differences between the AC approaches (>10%) occurred in cortical regions near the skull, including the occipital gyrus, inferior frontal cortex, orbitofrontal cortex, nucleus accumbens, and sensory and motor cortex. Small brain regions, such as the nucleus accumbens, also showed a high %ΔV_T difference between the two methods, which may be partially attributed to the noise of the PET images. In contrast, centrally located regions, including basal ganglia, the thalamus, and cingulate cortices, had lower differences (~5%). The difference in the estimated percentage occupancies (%Occ) between the two AC methods was smaller than the differences in the V_T values between the two AC methods. Collectively, the template-based AC method could increase the radioligand uptake by approximately 10% in macaque brains and quantitative outcomes (V_T) similarly. However, further studies are required to fully evaluate the potential benefits and drawbacks of the

https://doi.org/10.1021/acsomega.3c04824
ACS Omega 2023, 8, 45438−45446

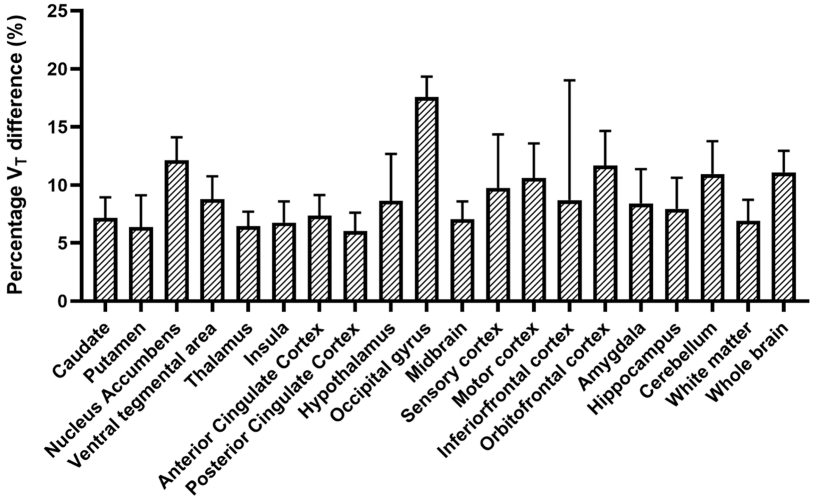

Figure 5. Regional percentage differences between the V_T values of the two AC methods ($V_{T,\ Template}$ and $V_{T,\ Segmentation}$) for all [^{18}F]PF-06455943 scans (n = 4). Volume of distribution, V_T; attenuation correction; AC.

template-based approach compared to CT- or transmission-based AC methods, which are termed a gold standard.

We compared the two AC methods to an [^{11}C]OMAR B/I scan with a within-scan rimonabant challenge to investigate whether the effects of an AC method on B/I PET studies with a drug challenge also have a similar impact. The reconstructed images of [^{11}C]OMAR in the units of SUV spanning 0−30 min were compared between the two AC approaches (Supporting Figure 2). The PET image reconstructed by segmentation-based AC showed a slightly lower [^{11}C]OMAR uptake, highlighted in the brain regions near the skull. Unlike the case of $SUV_{1-10\ min}$, lower nondisplaceable binding potential ($BP_{ND,baseline}$) values were shown with the template-based AC method than $BP_{ND,baseline}$ derived from the segmentation-based approach (Table S2). The estimated percent occupancy (%Occ) is larger in the template-based AC compared to that in the segmentation-based method across all ROIs (Figure 6). In the [^{18}F]PF-06455943 bolus studies, approximately 5−18% higher V_T values were shown with the template-based AC method, with increasing V_T values proximal to the skull, such as sensory, motor cortex, IFC, and OFC (Figure 5). Percent Occ of the [^{11}C]OMAR B/I study in brain regions close to the skull showed only moderately higher %Occ (∼5%) with the template-based AC compared to the segmentation AC, and brain regions with high CB1R density show higher %Occ (∼5−10%) with the template-based AC method. This discrepancy between bolus versus B/I studies could be explained by the fact that a reference-tissue method was used for the [^{11}C]OMAR B/I study, in which the reference region, the occipital gyrus, is one of the most sensitive regions to the effects of AC due to its proximity to the skull. Specifically, the overestimated $BP_{ND,baseline}$ of the segmentation-based AC led to lower %Occ compared with the template-based approach, suggesting that the interplay between the effects of the AC in a target and reference region may cause a regional bias in final measures that were used to evaluate the target engagement of a drug. Therefore, it is important to note that although one would expect that the AC method will introduce minimal bias and inaccuracy for within-scan challenge studies, our results demonstrated that an accurate AC is essential for PET studies using the reference tissue model without arterial blood samples, especially when the reference region is located near the skull.

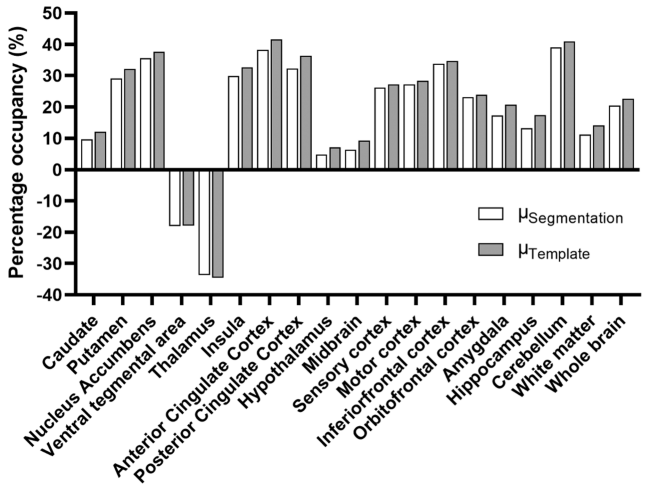

Figure 6. Regional %Occ for [^{11}C]OMAR, induced by a CB1R antagonist, rimonabant, obtained by using either template/segmentation-based AC method. Percentage occupancy, %Occ; cannabinoid 1 receptor, CB1R; attenuation correction, AC.

The effect of potential misregistration was simulated and tested in this study, particularly considering the facial bones within the NHP spout, the area most prone to misregistration errors (shown in Supporting Figure 3). Due to their inherently high anatomic variation and suboptimal performance of registration tools outside of the brain, misregistration can be expected to occur in these regions despite excellent registration over the brains and skull. The simulation in this study was an extreme case of misregistration, with the facial bones totally excluded, replacing their LACs with that of the soft tissue. Despite the apparent differences shown in the μ maps, the impact on the reconstructed PET images was negligible (∼1%), which can be explained by the fact that the lines of response traverse both the facial bones and the brain consist of only a tiny fraction of the reconstructed PET images, consistent with the previous study in the human brain.[15] These results suggest that the effects of misregistration in the facial bone will not hinder the advantage of the template-based AC method for PET/MR imaging in NHP brains.

https://doi.org/10.1021/acsomega.3c04824
ACS Omega 2023, 8, 45438−45446

Limitations. This study was not without limitations. First, the two MR-based AC methods were not directly validated against the gold-standard CT-based AC. However, a similar template-based MR-based AC method in the human brain has been validated against the CT-based AC method previously and showed minimal errors.[15] Although a complete validation with the gold-standard method was not applicable, we focused on the preliminary results that indicate the differences between AC methods for PET quantitative outcomes in the contexts of the two most common experiments in NHPs. To validate the accuracy of the AC methods without assumptions, a future study including the CT-based AC method for PET images would further validate the template-based AC for the NHP brain. In addition, the segmentation of the six tissue classes is less accurate in the facial bone and neck area of the NHPs, leading to less accurate μ maps in these regions. This is due to the large anatomical variation observed between the NHPs. The segmentation performance relies heavily on the prior anatomic information on the template. Since the registration to the template using a linear transformation was performed before tissue segmentation, the facial and neck regions could not be registered to the template with high accuracy. However, as shown in the simulation in this study, the inaccuracy in the template-based AC induced by the misregistration in facial bone regions has a minimal impact on the reconstructed PET image.

CONCLUSIONS

In conclusion, the template-based AC approach was successfully applied to PET data obtained by integrated PET/MR systems in the context of two typical PET applications on rhesus macaque brains. The population-based template from the ten NHPs was used to generate a pCT image from MRI images, and the performance was reliable despite large anatomic variations within macaques. Comparison with the segmentation-based approach revealed that applying the template-based AC could increase the SUV and V_T of [^{18}F]PF-06455943 by approximately 10% over the brain. The impact of misregistration within the facial bones was expected to be minor (~1%) for the template-based AC method. The ΔDBP_{ND} of [^{11}C]OMAR calculated by modified SRTM2 was slightly higher with the template-based AC than the segmentation-based method. However, unlike the case of [^{18}F]PF-06455943, where the effect of AC caused simple biases in V_T with an increase near the skull, a complicated regional bias was shown due to the interplay of the effects of AC between the target and reference regions in the brain. We thus believe that the template-based AC approach is appropriate for baseline-blocking studies with arterial blood sampling, but experiments requiring kinetic modeling *via* a reference region—such as B/I or nonarterial blood sampling experiments—require additional studies to validate and extend its utility in such scenarios, especially with a gold-standard AC method.

METHODS

Template Generation and Validation. CT and MRI images were acquired on ten adult rhesus macaques (weight range: 4.6–8.2 kg) at the PET/CT-MRI center in the First Affiliated Hospital of Jinan University to generate population-based CT and MRI templates. All procedures were approved by the local ethical committee (Animal Care and Use Committee of Guangdong Landau Biotechnology Co. Ltd., which was approved by the Association for Assessment and Accreditation of Laboratory Animal Care). CT images were acquired using a GE Discovery 690 PET/CT (GE Healthcare, Chicago, Illinois), field-of-view (FOV) = 50 cm; slice thickness = 2.5 mm; matrix size = 512 × 512; display FOV (DFOV) = 30 cm; window width/level = 100:35; adaptive statistical iterative reconstruction (ASiR) = 30%. T1-weighted three-dimensional (3D) magnetization-prepared rapid gradient echo (MPRAGE) MR images were acquired on a GE Discovery 750 3T MRI, with the following parameters: repetition time (TR) = 8.4 ms, echo time (TE) = 3.4 ms, inversion time (TI) = 450 ms, slice thickness = 1.1 mm, matrix size = 256 × 256, and FOV = 18 × 18 cm. Each macaque was anesthetized with ketamine (10 mg/kg, i.m.) and placed into the scanner in the head-first supine position, with their head fixed using a homemade acrylic holder.

MR and CT images from the same NHP were nonrigidly coregistered using ANTS software.[23] The template atlas was created by first segmenting the MR and CT image pair for each of the 10 NHPs in the atlas-generation data set into 6 tissue classes: white matter (WM), gray matter (GM), cerebrospinal fluid (CSF), bone, soft tissue, and air. A series of morphological operations were performed to ensure that the tissue class included the entire brain and reduced potential artifacts. Briefly, a brain-only mask combining the GM, WM, and CSF tissue probability maps was generated with a low threshold (0.2) to ensure the mask did not miss any potential voxels that were, in fact, brain voxels. The bone tissue probability maps were eroded to limit CSF voxels misclassified as bone. Eroded bone voxels were then assigned to the CSF class. Additionally, manual edits were made to the bone tissue probability maps to remove the head fixation device from the images. The voxels inside this final brain-only mask were zeroed in the bone probability map. The final tissue classes were then nonrigidly coregistered using SPM8 DARTEL to generate cohort-specific tissue class templates and a CT template. CT-like (pseudo-CT) images were obtained by applying the inverse transformation and converted to linear attenuation coefficients for the AC of PET data. The LOOCV approach was applied to validate the atlas-generation process of every NHP, comparing either μ maps obtained from the segmentation-based ($\mu_{Segmentation}$) or template-based AC method ($\mu_{Template}$) to the CT-driven μ map (μ_{CT}), using the remaining nine data sets used to create an NHP subject-specific template.

PET/MR Data Acquisition. To validate the performance of the template-based AC, we included two PET/MR data sets in a separate cohort of rhesus macaques (N = 4; weight: 9.3 ± 1.1 kg) for translational applications in the NHP brain. First, in the context of PET studies for evaluating a novel radiotracer, [^{18}F]PF-06455943 PET scans were acquired (two baselines and two self-blocking scans) with arterial blood sampling. Second, a B/I PET scan of [^{11}C]OMAR was performed with a dose of the CB1R antagonist administered during image acquisition. All PET and MRI images were obtained using a 3T Siemens TIM-Trio with a BrainPET insert (Siemens, Erlangen, Germany). A custom-built 8-channel PET/MRI compatible array coil dedicated to NHP brain imaging was used to enhance the signal intensity and quality of images. For the [^{18}F]PF-06455943 PET scans, dynamic 120 min acquisition was initiated together with a bolus injection of ~200 MBq (196.47 ± 8.23 MBq averaged from 4 scans) of [18F]PF-

https://doi.org/10.1021/acsomega.3c04824
ACS Omega 2023, 8, 45438−45446

06455943 over 30 s to the animal. For the blocking scans, unlabeled PF-06455943 (0.1 or 0.3 mg/kg; 10% DMSO/10% Tween 80/Saline (V/V)) was intravenously injected to NHP approximately 10 min before the injection of the radiotracer. For the [^{11}C]OMAR B/I scan, 100 min of dynamic PET scanning was obtained with a Kbol of ∼150 min of [^{11}C]OMAR. At 40 min post radiotracer injection, Rimonabant (3 mg/kg), a CB1R antagonist, was injected intravenously. The acquired list mode data were reconstructed using the 3D ordinary Poisson expectation-maximization algorithm (16 subsets and 6 iterations) with detector efficiency, decay, dead time, random coincidences, and scatter and attenuation corrections (see below). [^{18}F]PF-06455943 PET images were dynamically reconstructed into the following frames to account for the biological distribution of the tracer and radioactive decay: 6 × 10, 6 × 20, 2 × 30, 1 × 1, 5 × 5, and 9 × 10 min. In contrast, constant intervals (50 × 120 s) were used for [^{11}C]OMAR PET reconstruction. All images were reconstructed into 153 slices with 256 × 256 pixels and 1.25 mm isotropic voxel size. In addition to PET image concentration, in Bq/ml, images were converted into SUV with body weight normalization. Simultaneously to PET image acquisition, high-resolution structural MRI scans were acquired by using multiecho-MPRAGE (ME-MPRAGE) sequence with parameters as follows: TR = 2400 ms; TE1/TE2/TE3/TE4 = 1.57/3.29/5.01/6.73 ms; TI = 1200 ms; flip angle = 9°; spatial resolution = 1 mm isotropic.

Attenuation Correction. To compare the template-based AC method with a segmentation-based AC for NHP brain PET imaging,[22] we reconstructed PET data using either μ maps obtained from the segmentation-based ($\mu_{\text{Segmentation}}$) or template-based AC method (μ_{Template}). Other than attenuation correction, all corrections and processing were identical between the two reconstructions.

CT-Based AC (Atlas-Generation Only). The CT images registered to the MR images of the atlas-generation data set were used to serve as gold-standard validation on the LOOCV. CT images of Hounsfield units were converted into LACs using a bilinear transformation[24] to generate the gold-standard μ_{CT}.

Segmentation-Based AC. In the case of the segmentation-based AC, a contour of the head, neck, and shoulders of the NHP was obtained by thresholding a preliminary PET image reconstructed by the filtered back-projection algorithm. A LAC value of water (0.096 cm^{-1}) was homogeneously assigned to the created contour and used to generate the mu map by adding the predefined coil structures. As previously reported,[22] this method, misclassifying the air cavity and bone as water, was likely better than most calculated AC methods despite bias.

Template-Based AC. For the template-based AC approach, the MR image was first preprocessed by the following steps, which was essential to account for low MR intensity around the neck and shoulder and intensity biases. Structural MR images were intensity-normalized using FreeSurfer[25] and ANTs[26] with a contour mask including the head, neck, and shoulders of the NHP applied. The preprocessed image was registered to the NMT NHP brain template using a linear affine registration with 12 degree-of-freedom[27] before tissue segmentation. Using SPM8 and the tissue probability map generated from the atlas-generation step, we segmented the image into six classes. Nonlinear registration was performed on the tissue classes to warp each class to the previously created template using the SPM8 DARTEL algorithm. Finally, the CT template image was inversely warped into subject space using SPM8, and its Hounsfield units were converted to LACs by using a bilinear transformation. A 4 mm Gaussian kernel spatially smoothed the generated LAC map to match the PET spatial resolution, and the predefined coil structures were added to generate the final μ_{Template}.

Lastly, we tested the impact of misregistration between the template-based AC and PET/MR data on the [^{18}F]PF-06455943 data set. Potential misregistration cases could arise in the facial bone regions due to the naturally increased anatomical variability among our NHPs in this area, especially between the atlas-generation and the validation data sets due to the large size difference across animals. To simulate large misregistration cases, the LAC values in the facial bone regions from the template-based method were replaced by the soft-tissue value, 0.096 cm^{-1} ($\mu_{\text{Misregistration}}$).

Quantitative PET Analysis. All PET scans with the different AC approaches were registered to the INIA19 Primate Brain Atlas[21] using JIP tools optimized for NHP data processing (www.nitrc.org/projects/jip). The high-resolution T1-weighted MRI image, which was coregistered with the PET data, was first affinity-registered to the INIA19 atlas. The resulting transformation matrix was applied to the dynamic PET data. Spatial smoothing with a 4 mm fwhm Gaussian kernel was applied to the PET data after the registration to the INIA19 template. Utilizing the INIA19 atlas, 20 regions of interest (ROIs) were defined to derive regional time-activity curves (TACs). These ROIs include caudate, putamen, nucleus accumbens, ventral tegmental area, thalamus, hypothalamus, amygdala, hippocampus, insula, anterior cingulate cortex, posterior cingulate cortex, occipital gyrus, midbrain, sensory cortex, motor cortex, inferior frontal cortex, orbitofrontal cortex, whole cerebellum, and white matter. In addition, a whole-brain ROI was used to calculate the whole-brain mean value. We performed kinetic modeling analysis for the [^{18}F]PF-06455943 scans using PMOD, 3.9 (PMOD Technologies Ltd., Zurich, Switzerland). The 2TCM was used to estimate the V_{T} for [^{18}F]PF-06455943 with the metabolite-corrected arterial plasma data, with the assumption that the blood volume is a constant (5%) for all ROIs. In the previous study, the 2TCM was determined to be the most suitable model for quantitative mapping of [^{18}F]PF-06455943.[19,20] Occupancies (%Occ) with unlabeled PF-06455943 were calculated by dividing the reduction of [^{18}F]PF-06455943 V_{T} value by homologous blocking with 0.1 or 0.3 mg/kg of unlabeled PF-06455943 ($V_{\text{T, Baseline}} - V_{\text{T, Blocking}}$) by the baseline V_{T} value, respectively. For [^{11}C]OMAR B/I analysis, the JIP tools were used to calculate the nondisplaceable binding potential before ($\text{BP}_{\text{ND, Baseline}}$) and after ($\text{BP}_{\text{ND, Blocking}}$) rimonabant challenge using the occipital gyrus as a reference region. The occipital gyrus was used as a pseudoreference tissue for [^{11}C]OMAR to calculate BP_{ND} using SRTM2 because it was a brain region with the lowest [^{11}C]OMAR binding (data not shown). %Occ was estimated by dividing the displacement of [^{11}C]OMAR induced by rimonabant ($\text{BP}_{\text{ND, Baseline}} - \text{BP}_{\text{ND, Blocking}}$) by the before challenge of [^{11}C]OMAR binding ($\text{BP}_{\text{ND, Baseline}}$), as described in previous studies.[9,10,28]

Comparison between Attenuation Corrections. For the LOOCV, comparing either μ_{Template} or $\mu_{\text{Segmentation}}$ to μ_{CT}, an absolute percentage difference (%PD) was defined as follows

https://doi.org/10.1021/acsomega.3c04824
ACS Omega 2023, 8, 45438−45446

$$\%PD = |(\mu_{template\ or\ segmentation} - \mu_{CT})/\mu_{CT} \times 100| \quad (1)$$

For a voxel-based comparison of the [^{18}F]PF-06455943 data set, the PET images from one to ten min post radiotracer injection ($SUV_{1-10\ min}$) reconstructed *via* either method were used to calculate a percentage difference in uptake (%ΔSUV), as follows

$$\%\Delta SUV = (SUV_{1-10min,template} - SUV_{1-10min,segmentation}) / SUV_{1-10min,segmentation} \times 100 \quad (2)$$

For a region-based comparison, the regional V_T values for [^{18}F]PF-06455943 and %Occ of [^{11}C]OMAR were compared between the two AC methods. The percentage difference in V_T ($\%\Delta V_{T,\ Template\text{-}Segmentation}$) of the two AC methods was calculated as follows:

$$\%\Delta V_{T,template-threshold} = (V_{T,Template} - V_{T,segmentation})/V_{T,Segmentation} \times 100 \quad (3)$$

Finally, for a voxel-based comparison between the template-based method with/without misregistration of the facial bone and tissue outside of the brain, the $SUV_{1-10\ min}$ image of the [^{18}F]PF-06455943 was compared

$$\%\Delta SUV = (SUV_{1-10min,template} - SUV_{1-10min,misregistration}) / SUV_{1-10min,misregistration} \times 100 \quad (4)$$

■ ASSOCIATED CONTENT

Supporting Information

The Supporting Information is available free of charge at https://pubs.acs.org/doi/10.1021/acsomega.3c04824.

Bland−Altman plots for the voxel-based analyses for all validation subjects, comparing μ_{CT} and $\mu_{Template}$ (Figure S1); comparison of PET images reconstructed with the 2 AC methods ($PET_{Template}$ and $PET_{Segmentation}$) for a [^{11}C]OMAR scan spanning 0−30 min (top and middle row) and their percentage differences (bottom row), positron emission tomography, PET; attenuation correction, AC; standard uptake value, SUV (Figure S2); attenuation maps derived from the template-based AC ($\mu_{Template}$) and a version of the facial bones excluded ($\mu_{Misregireation}$), and their percentage differences in the reconstructed [^{18}F]PF-06455943 PET images, attenuation correction, AC; positron emission tomography, PET; linear attenuation coefficient, LAC; summary of the regional analysis for [^{18}F]PF-06455943 baseline and homologous blocking scans, abbreviations: NHP = nonhuman primate; AC = attenuation correction; V_T = volume of distribution; %Occ = percentage occupancy; NAc = nucleus accumbens; VTA = ventral tegmental area; ACC = anterior cingulate cortex; PCC posterior cingulate cortex; IFC = inferior frontal cortex; OFC = orbitofrontal cortex (Table S1); summary of the regional analysis for [^{11}C]OMAR B/I scan with rimonabant challenge, abbreviations: B/I = bolus plus infusion; BP_{ND} = nondisplaceable binding potential; %Occ = percentage occupancy; AC = attenuation correction; V_T = volume of distribution; NAc = nucleus accumbens; VTA = ventral tegmental area; ACC = anterior cingulate cortex; PCC posterior cingulate cortex; IFC = inferior frontal cortex; OFC = orbitofrontal cortex (Table S2) (PDF)

■ AUTHOR INFORMATION

Corresponding Authors

David Izquierdo-Garcia − *Athinoula A. Martinos Center for Biomedical Imaging, Department of Radiology, Massachusetts General Hospital, Harvard Medical School, Charlestown 02129, United States; Harvard−MIT Division of Health Sciences and Technology, Cambridge, Massachusetts 02139, United States; Bioengineering Department, Universidad Carlos III de Madrid, Madrid 28911, Spain*; Email: dizquierdogarcia@mgh.harvard.edu

Hsiao-Ying Wey − *Athinoula A. Martinos Center for Biomedical Imaging, Department of Radiology, Massachusetts General Hospital, Harvard Medical School, Charlestown 02129, United States*; orcid.org/0000-0002-1425-8489; Email: hsiaoying.wey@mgh.harvard.edu

Authors

Chi-Hyeon Yoo − *Athinoula A. Martinos Center for Biomedical Imaging, Department of Radiology, Massachusetts General Hospital, Harvard Medical School, Charlestown 02129, United States*

Jonathan M. DuBois − *Athinoula A. Martinos Center for Biomedical Imaging, Department of Radiology, Massachusetts General Hospital, Harvard Medical School, Charlestown 02129, United States*

Lu Wang − *Department of Nuclear Medicine and PET/CT-MRI Center, The First Affiliated Hospital of Jinan University, Guangzhou 510630, China*; orcid.org/0000-0002-8049-1991

Yongjin Tang − *Department of Nuclear Medicine and PET/CT-MRI Center, The First Affiliated Hospital of Jinan University, Guangzhou 510630, China*

Lu Hou − *Department of Nuclear Medicine and PET/CT-MRI Center, The First Affiliated Hospital of Jinan University, Guangzhou 510630, China*

Hao Xu − *Department of Nuclear Medicine and PET/CT-MRI Center, The First Affiliated Hospital of Jinan University, Guangzhou 510630, China*

Jiahui Chen − *Division of Nuclear Medicine and Molecular Imaging, Center for Advanced Medical Imaging Sciences, Department of Radiology, Massachusetts General Hospital, Harvard Medical School, Boston, Massachusetts 02114, United States*

Steven H. Liang − *Division of Nuclear Medicine and Molecular Imaging, Center for Advanced Medical Imaging Sciences, Department of Radiology, Massachusetts General Hospital, Harvard Medical School, Boston, Massachusetts 02114, United States*; orcid.org/0000-0003-1413-6315

Complete contact information is available at: https://pubs.acs.org/10.1021/acsomega.3c04824

Author Contributions

#C.-H.Y., J.M.D., and L.W. contributed equally to this work. C.Y. performed PET data reconstruction and kinetic modeling analysis and drafted the manuscript. J.D. performed PET/CT data analysis and drafted the manuscript. L.W., Y.T., and H.X. acquired PET/CT data and drafted the manuscript. J.C. prepared the radioligand [^{18}F]PF-06455943. S.L., D.I.-G., and

https://doi.org/10.1021/acsomega.3c04824
ACS Omega 2023, 8, 45438−45446

H.-Y.W. conceptualized and designed the study. All authors contributed to drafting and revising the manuscript.

Notes

The authors declare no competing financial interest.

■ ACKNOWLEDGMENTS

The authors declare no competing financial interests. The authors thank Grae Arabasz, Shirley Hsu, Regan Butterfield, and Oliver Ramsay for their assistance with radiotracer administration, Helen Deng for animal preparation and monitoring, and the Radiopharmacy at the Martinos Center for Biomedical Imaging for support in processing arterial blood samples. The study was, in part, supported by National Institutes of Health (NIH) grants R00DA037928 and R21DA047133 to H.-Y.W., and RF1AG073428, R01MH128705, R21AG074218, and R21AG078058 to S.H.L. Funding for the imaging facilities and infrastructure used in this work was provided by NIH grants S10RR017208, S10RR026666, S10RR022976, S10RR019933, S10RR023401, and S10OD023517.

■ REFERENCES

(1) Deng, X.; Rong, J.; Wang, L.; Vasdev, N.; Zhang, L.; Josephson, L.; Liang, S. H. Chemistry for Positron Emission Tomography: Recent Advances in 11 C-, 18 F-, 13 N-, and 15 O-Labeling Reactions. *Angew. Chem., Int. Ed.* **2019**, *58*, 2580−2605, DOI: 10.1002/anie.201805501.

(2) Takano, A.; Varrone, A.; Gulyás, B.; Salvadori, P.; Gee, A.; Windhorst, A.; Vercouillie, J.; Bormans, G.; Lammertsma, A. A.; Halldin, C. Guidelines to PET Measurements of the Target Occupancy in the Brain for Drug Development. *Eur. J. Nucl. Med. Mol. Imaging* **2016**, *43*, 2255−2262, DOI: 10.1007/s00259-016-3476-4.

(3) Takamura, Y.; Kakuta, H. In Vivo Receptor Visualization and Evaluation of Receptor Occupancy with Positron Emission Tomography. *J. Med. Chem.* **2021**, *64*, 5226−5251, DOI: 10.1021/acs.jmedchem.0c01714.

(4) Zhang, Y.-p.; Shi, L.m. Phylogeny of Rheusus Monkeys (Macaca Mulatta) as Revealed by Mitochondrial DNA Restriction Enzyme Analysis. *Int. J. Primatol.* **1993**, *14*, 587−605, DOI: 10.1007/BF02215449.

(5) Chen, Y.; An, H. Attenuation Correction of PET/MR Imaging. *Magn. Resonance Imaging Clin. North Am.* **2017**, *25*, 245−255, DOI: 10.1016/j.mric.2016.12.001.

(6) Disselhorst, J. A.; Bezrukov, I.; Kolb, A.; Parl, C.; Pichler, B. J. Principles of PET/MR Imaging. *J. Nucl. Med.* **2014**, *55*, 2S−10S, DOI: 10.2967/jnumed.113.129098.

(7) Catana, C. Principles of Simultaneous PET/MRImaging. *Magn. Reson. Imaging Clin. North Am.* **2017**, *25*, 231−243, DOI: 10.1016/j.mric.2017.01.002.

(8) Chen, K. T.; Salcedo, S.; Chonde, D. B.; Izquierdo-Garcia, D.; Levine, M. A.; Price, J. C.; Dickerson, B. C.; Catana, C. MR-Assisted PET Motion Correction in Simultaneous PET/MRI Studies of Dementia Subjects. *J. Magn. Reson. Imaging* **2018**, *48*, 1288−1296, DOI: 10.1002/jmri.26000.

(9) Mandeville, J. B.; Sander, C. Y. M.; Jenkins, B. G.; Hooker, J. M.; Catana, C.; Vanduffel, W.; Alpert, N. M.; Rosen, B. R.; Normandin, M. D. A Receptor-Based Model for Dopamine-Induced FMRI Signal. *NeuroImage* **2013**, *75*, 46−57, DOI: 10.1016/j.neuroimage.2013.02.036.

(10) Sander, C. Y.; Hooker, J. M.; Catana, C.; Normandin, M. D.; Alpert, N. M.; Knudsen, G. M.; Vanduffel, W.; Rosen, B. R.; Mandeville, J. B. Neurovascular Coupling to D2/D3 Dopamine Receptor Occupancy Using Simultaneous PET/Functional MRI. *Proc. Natl. Acad. Sci. U.S.A.* **2013**, *110*, 11169−11174, DOI: 10.1073/pnas.1220512110.

(11) Wey, H. Y.; Catana, C.; Hooker, J. M.; Dougherty, D. D.; Knudsen, G. M.; Wang, D. J. J.; Chonde, D. B.; Rosen, B. R.; Gollub, R. L.; Kong, J. Simultaneous FMRI-PET of the Opioidergic Pain System in Human Brain. *NeuroImage* **2014**, *102*, 275−282, DOI: 10.1016/j.neuroimage.2014.07.058.

(12) Villien, M.; Wey, H. Y.; Mandeville, J. B.; Catana, C.; Polimeni, J. R.; Sander, C. Y.; Zürcher, N. R.; Chonde, D. B.; Fowler, J. S.; Rosen, B. R.; Hooker, J. M. Dynamic Functional Imaging of Brain Glucose Utilization Using FPET-FDG. *NeuroImage* **2014**, *100*, 192−199, DOI: 10.1016/j.neuroimage.2014.06.025.

(13) Sander, C. Y.; Hansen, H. D.; Wey, H. Y. Advances in Simultaneous PET/MR for Imaging Neuroreceptor Function. *J. Cereb. Blood Flow Metab.* **2020**, *40*, 1148−1166, DOI: 10.1177/0271678X20910038.

(14) Roy, S.; Wang, W. T.; Carass, A.; Prince, J. L.; Butman, J. A.; Pham, D. L. PET Attenuation Correction Using Synthetic CT from Ultrashort Echo-Time MR Imaging. *J. Nucl. Med.* **2014**, *55*, 2071−2077, DOI: 10.2967/jnumed.114.143958.

(15) Izquierdo-Garcia, D.; Hansen, A. E.; Förster, S.; Benoit, D.; Schachoff, S.; Fürst, S.; Chen, K. T.; Chonde, D. B.; Catana, C. An SPM8-Based Approach for Attenuation Correction Combining Segmentation and Nonrigid Template Formation: Application to Simultaneous PET/MR Brain Imaging. *J. Nucl. Med.* **2014**, *55*, 1825−1830, DOI: 10.2967/jnumed.113.136341.

(16) Mehranian, A.; Arabi, H.; Zaidi, H. Quantitative Analysis of MRI-Guided Attenuation Correction Techniques in Time-of-Flight Brain PET/MRI. *NeuroImage* **2016**, *130*, 123−133, DOI: 10.1016/j.neuroimage.2016.01.060.

(17) Catana, C.; Laforest, R.; An, H.; Boada, F.; Cao, T.; Faul, D.; Jakoby, B.; Jansen, F. P.; Kemp, B. J.; Kinahan, P. E.; Larson, P.; Levine, M. A.; Maniawski, P.; Mawlawi, O.; McConathy, J. E.; McMillan, A. B.; Price, J. C.; Rajagopal, A.; Sunderland, J.; Veit-Haibach, P.; Wangerin, K. A.; Ying, C.; Hope, T. A. A Path to Qualification of PET/MRI Scanners for Multicenter Brain Imaging Studies: Evaluation of MRI-Based Attenuation Correction Methods Using a Patient Phantom. *J. Nucl. Med.* **2022**, *63*, 615−621, DOI: 10.2967/jnumed.120.261881.

(18) Ladefoged, C. N.; Law, I.; Anazodo, U.; St Lawrence, K.; Izquierdo-Garcia, D.; Catana, C.; Burgos, N.; Cardoso, M. J.; Ourselin, S.; Hutton, B.; Mérida, I.; Costes, N.; Hammers, A.; Benoit, D.; Holm, S.; Juttukonda, M.; An, H.; Cabello, J.; Lukas, M.; Nekolla, S.; Ziegler, S.; Fenchel, M.; Jakoby, B.; Casey, M. E.; Benzinger, T.; Højgaard, L.; Hansen, A. E.; Andersen, F. L. A Multi-Centre Evaluation of Eleven Clinically Feasible Brain PET/MRI Attenuation Correction Techniques Using a Large Cohort of Patients. *NeuroImage* **2017**, *147*, 346−359, DOI: 10.1016/j.neuroimage.2016.12.010.

(19) Chen, Z.; Chen, J.; Chen, L.; Yoo, C. H.; Rong, J.; Fu, H.; Shao, T.; Coffman, K.; Steyn, S. J.; Davenport, A. T.; Daunais, J. B.; Haider, A.; Collier, L.; Josephson, L.; Wey, H. Y.; Zhang, L.; Liang, S. H. Imaging Leucine-Rich Repeat Kinase 2 in Vivo with 18F-Labeled Positron Emission Tomography Ligand. *J. Med. Chem.* **2022**, *2*, 1712−1724, DOI: 10.1021/acs.jmedchem.2c00551.

(20) Yoo, C.-H.; Chen, Z.; Rani, N.; Chen, J.; Rong, J.; Chen, L.; Zhang, L.; Liang, S. H.; Wey, H.-Y. Evaluation of [(18)F]PF-06455943 as a Potential LRRK2 PET Imaging Agent in the Brain of Nonhuman Primates. *ACS Chem. Neurosci.* **2023**, *14* (3), 370−377.

(21) Rohlfing, T.; Kroenke, C. D.; Sullivan, E. V.; Dubach, M. F.; Bowden, D. M.; Grant, K. A.; Pfefferbaum, A. The INIA19 Template and NeuroMaps Atlas for Primate Brain Image Parcellation and Spatial Normalization. *Front. Neuroinform.* **2012**, *6*, No. 27, DOI: 10.3389/fninf.2012.00027.

(22) Catana, C.; Van Der Kouwe, A.; Benner, T.; Michel, C. J.; Hamm, M.; Fenchel, M.; Fischl, B.; Rosen, B.; Schmand, M.; Sorensen, A. G. Toward Implementing an MRI-Based PET Attenuation-Correction Method for Neurologic Studies on the MR-PET Brain Prototype. *J. Nucl. Med.* **2010**, *51*, 1431−1438, DOI: 10.2967/jnumed.109.069112.

https://doi.org/10.1021/acsomega.3c04824
ACS Omega 2023, 8, 45438−45446

(23) Avants, B. B.; Tustison, N. J.; Song, G.; Cook, P. A.; Klein, A.; Gee, J. C. A Reproducible Evaluation of ANTs Similarity Metric Performance in Brain Image Registration. *NeuroImage* **2011**, *54*, 2033−2044, DOI: 10.1016/j.neuroimage.2010.09.025.
(24) Burger, C.; Goerres, G.; Schoenes, S.; Buck, A.; Lonn, A.; Von Schulthess, G. PET Attenuation Coefficients from CT Images: Experimental Evaluation of the Transformation of CT into PET 511-KeV Attenuation Coefficients. *Eur. J. Nucl. Med.* **2002**, *29*, 922−927, DOI: 10.1007/s00259-002-0796-3.
(25) Dale, A. M.; Fischl, B.; Sereno, M. I. Cortical Surface-Based Analysis: I. Segmentation and Surface Reconstruction. *NeuroImage* **1999**, *9*, 179−194, DOI: 10.1006/nimg.1998.0395.
(26) Tustison, N. J.; Avants, B. B.; Cook, P. A.; Zheng, Y.; Egan, A.; Yushkevich, P. A.; Gee, J. C. N4ITK: Improved N3 Bias Correction. *IEEE Trans. Med. Imaging* **2010**, *29*, 1310−1320, DOI: 10.1109/TMI.2010.2046908.
(27) Seidlitz, J.; Sponheim, C.; Glen, D.; Ye, F. Q.; Saleem, K. S.; Leopold, D. A.; Ungerleider, L.; Messinger, A. A Population MRI Brain Template and Analysis Tools for the Macaque. *NeuroImage* **2018**, *170*, 121−131, DOI: 10.1016/j.neuroimage.2017.04.063.
(28) Wey, H. Y.; Wang, C.; Schroeder, F. A.; Logan, J.; Price, J. C.; Hooker, J. M. Kinetic Analysis and Quantification of [11C]-Martinostat for in Vivo HDAC Imaging of the Brain. *ACS Chem. Neurosci.* **2015**, *6*, 708−715, DOI: 10.1021/acschemneuro.5b00066.

https://doi.org/10.1021/acsomega.3c04824
ACS Omega 2023, 8, 45438−45446